Journal of Rock Mechanics and Geotechnical Engineering 16 (2024) 661–669

Contents lists available at ScienceDirect

Journal of Rock Mechanics and Geotechnical Engineering

journal homepage: www.jrmge.cn

Full Length Article

Biomineralization and mineralization using microfluidics: A comparison study

Yang Xiao [a,b,c], Xiang He [d,*], Guoliang Ma [a,c], Chang Zhao [a,c], Jian Chu [d], Hanlong Liu [a,b,c]

[a] Key Laboratory of New Technology for Construction of Cities in Mountain Area, Chongqing University, Chongqing, 400045, China
[b] State Key Laboratory of Coal Mine Disaster Dynamics and Control, Chongqing University, Chongqing, 400045, China
[c] School of Civil Engineering, Chongqing University, Chongqing, 400045, China
[d] School of Civil and Environmental Engineering, Nanyang Technological University, Singapore

ARTICLE INFO

Article history:
Received 26 November 2022
Received in revised form
5 February 2023
Accepted 12 March 2023
Available online 17 July 2023

Keywords:
Microbially induced carbonate precipitation (MICP)
Biocementation
Crystal
Calcium carbonate
Nucleation

ABSTRACT

Biomineralization through microbial process has attracted great attention in the field of geotechnical engineering due to its ability to bind granular materials, clog pores, and seal fractures. Although minerals formed by biomineralization are generally the same as that by mineralization, their mechanical behaviors show a significant discrepancy. This study aims to figure out the differences between biomineralization and mineralization processes by visualizing and tracking the formation of minerals using microfluidics. Both biomineralization and mineralization processes occurred in the Y-shaped sand-containing microchip that mimics the underground sand layers. Images from different areas in the reaction microchannel of microchips were captured to directly compare the distribution of minerals. Crystal size and numbers from different reaction times were measured to quantify the differences between biomineralization and mineralization processes in terms of crystal kinetics. Results showed that the crystals were precipitated in a faster and more uncontrollable manner in the mineralization process than that in the biomineralization process, given that those two processes presented similar precipitation stages. In addition, a more heterogeneous distribution of crystals was observed during the biomineralization process. The precipitation behaviors were further explained by the classical nucleation crystal growth theory. The present microfluidic tests could advance the understanding of biomineralization and provide new insight into the optimization of biocementation technology.

1. Introduction

Biomineralization is an important natural resource that forms minerals during the earth element recycle process. Microbially induced carbonate precipitation (MICP), a paradigm of biomineralization, has attracted great attention in the revolution of civil engineering that seeks for lower carbon emission, energy saving, and environmental solutions in the recent decades (Mitchell and Santamarina, 2005; DeJong et al., 2013; Terzis and Laloui, 2019). The carbonate minerals precipitated in the porous media could significantly alter the mechanical properties through biocementation and bioclogging effects (Chu et al., 2014; Ma et al., 2021). This includes improvement of strength (Montoya and DeJong, 2015; Xiao et al., 2019a; Sharma et al., 2021), decrease of permeability (Chu et al., 2013; Zamani et al., 2019), increase of stiffness and dilatancy (Montoya and DeJong, 2015; Xiao et al., 2019b), improvement of liquefaction resistance (Simatupang et al., 2018; Xiao et al., 2018; Lee et al., 2022; Sharma et al., 2022), and mitigation of erosion (Dagliya et al., 2022). For this, the MICP technique has a potential in the various geotechnical applications, such as pile engineering (Lin et al., 2016; Xiao et al., 2020), shallow foundation (San Pablo et al., 2020; Montoya et al., 2021), slope engineering (Salifu et al., 2016; Xiao et al., 2022a), subgrade engineering (Porter et al., 2018; Xiao et al., 2022b), underground seepage control engineering (Cuthbert et al., 2013; Kirkland et al., 2020), and heavy metal immobilization (Sharma et al., 2020). Considerable efforts have been made to advance the understanding of MICP. The mechanisms involved in the MICP process, however, are far less studied, partly due to a lack of the miniaturized model systems that could visualize the process at high spatial and temporal resolutions.

* Corresponding author. School of Civil and Environmental Engineering, Nanyang Technological University, Singapore.
E-mail address: xiang.he@ntu.edu.sg (X. He).

Peer review under responsibility of Institute of Rock and Soil Mechanics, Chinese Academy of Sciences.

https://doi.org/10.1016/j.jrmge.2023.03.019

Microfluidic device, due to its optical transparency and controllable manner in fluids, has been widely used to investigate the crystallization (Gong et al., 2015; He et al., 2020) and microorganisms' behaviors (Dehkharghani et al., 2019; de Anna et al., 2020). The microfluidics has been used in previous studies to characterize the pore-scale behaviors of the MICP process (Wang et al., 2019a; Zambare et al., 2020; Xiao et al., 2021). Wang et al. (2019a) employed a polydimethylsiloxane (PDMS) fabricated porous microfluidic chip to observe the crystal growth among pore spaces. They further used this chip to investigate the factors (e.g. bacterial density and concentrations of cementation solution) that affect the particle-scale characteristics of precipitates (Wang et al., 2019b, 2021). Assuming that the bacterial cells are enveloped by calcite crystals for the two-step injection method, Marzin et al. (2020) evaluated the adhesion rate of bacteria by directly counting crystals on the sandstone grains. Kim et al. (2020) proposed a calcium carbonate ($CaCO_3$) growth model for the homogeneous microfluidic chip and applied the model to studying the enzymatically induced $CaCO_3$ precipitation process. Xiao et al. (2022a) investigated the bacterial diffusion and the $CaCO_3$ distribution through microfluidics at various concentrations of calcium ions.

These studies have provided new insights on understanding the microscale behaviors of MICP and have demonstrated the great advantages of the microfluidic technology. However, most of previous studies use a pure PDMS microchip without sand particles, which might cause disparities between real situations (MICP among sand particles) and model test (PDMS formed porous media). Besides, the lack of direct comparison between MICP and chemically induced carbonate precipitation (CICP) obstacles the application of crystal nucleation and growth theories that have been fully understood for the calcium carbonate crystallization. Calcium carbonate can be synthesized through both biomineralization (e.g. MICP) and mineralization processes (e.g. CICP). For both processes, the calcium carbonate minerals are formed by combing calcium ions and carbonate ions and precipitated in alkaline environment. The main difference in ingredients between MICP and CICP is the sources of carbonate. For the MICP process, carbonate ions are produced by the hydrolysis of urea through bacterial catalysis. The alkaline environment is also created during the hydrolyzing of urea. Contrary to MICP, the carbonate ions in CICP process are provided by adding dissolved carbonate salts, such as sodium carbonate, without addition of the external enzyme or catalyst. The detailed CICP reactions are given as follows:

$$CO_3^{2-} + H_2O \leftrightarrow HCO_3^- + OH^- \tag{1a}$$

$$HCO_3^- + H_2O \leftrightarrow H_2CO_3 + OH^- \tag{1b}$$

$$Ca^{2-} + CO_3^{2-} \rightarrow CaCO_3\downarrow \tag{1c}$$

As presented in Eqs. (1a)-(1c), the dissolved carbonate would partially react with water molecule, leading to an elevation of solution's pH value. The existing calcium ions combined with the carbonate and precipitated calcium carbonate in alkaline environment.

This study compares the evolution processes of MICP and CICP to characterize the distribution of precipitates, followed by quantifying the number of crystals during reaction. Moreover, the nucleation behaviors are analyzed based on the classical nucleation theory. The present study gives new insight into the understanding of the MICP process and would facilitate manipulating the MICP process in a more controllable and effective way.

2. Material and methods

2.1. Visualization platform

The visualization of mineral-carbonation was achieved using a microfluidic platform, which mainly consists of three subsystems: injection subsystem, microchip, and observation subsystem (see Fig. A1). More details of the microfluidic platform can be found in Xiao et al. (2022c). The injection subsystem was used for delivering solutions into the microchip. The main device of this subsystem is a dual-channel syringe pump (Harvard Pump 11 Elite 4501, USA), which ensures a simultaneous injection of two solutions. The microchip provides the environment where the mineral-carbonation occurs. A custom-designed microchip, i.e. sand-containing microchip, was constructed to mimic the environment where saturated sands were cemented by minerals. The detailed fabrication procedures will be described in Section 2.3. The observation subsystem contains an inverted microscope (Olympus IX73, Japan) equipped with an s-COMS camera (Olympus DP74, Japan) and a computer, which enables a continuous real-time imaging and acquisition for the reactions. The microfluidic platform was insulated in an isolation box to maintain a constant temperature and avoid light interference.

2.2. Bacterial suspension and chemical solutions

An alkaliphilic strain, Sporosarcina Pasteurii (American Type Culture Collection 11859), was used as model microorganism for biomineralization. The cultivation and associated harvest procedures of bacterial suspension could be found in Xiao et al. (2021). The urease activity of bacterial suspension was measured before the initiation of biomineralization. The bacterial suspension with a urease activity of 10 U was attained by diluting the harvest bacteria with 0.85% (weight per volume) NaCl solution. The bacterial suspension was used immediately after dilution as the urease activity decreased due to stock. Two cementation solutions were used for biomineralization; both were composed of $CaCl_2$ and urea, with the urea concentration of 0.5 mol/L. For the test with high concentration of Ca^{2+}, denoted as MICP1, the concentration of $CaCl_2$ was 0.5 mol/L; while for the test with low concentration, denoted as MICP2, the concentration of $CaCl_2$ was 0.05 mol/L. For the mineralization test, denoted as CICP, equimolar aqueous solutions of $CaCl_2$ and Na_2CO_3 were used with a concentration of 0.5 mol/L. Table 1 shows the chemicals used for the microfluidic tests. All chemical materials were in analytic grade and dissolved in deionized water to prepare the solutions.

2.3. Fabrication of sand-containing microchip

The sand-containing microchip was composed of a PDMS groove, sand particles, and a PDMS plate. The PDMS groove has a Y-shaped pattern as shown in Fig. 1a. The dimensions of this pattern are 120 μm in depth, 950 μm in width, and 8000 μm in length. The PDMS groove was fabricated using photolithography technique. Details of the fabrication of PDMS groove and plate were discussed in Xiao et al. (2022c). Sand particles were sieved from Fujian sand. Those retained on the meshes of 0.1 mm and 0.15 mm were used for the microchip. The sand particles were placed manually by tweezer

Table 1
Chemicals for the microfluidic tests.

Test ID	Bacterial suspension	Urea (mol/L)	Na_2CO_3 (mol/L)	$CaCl_2$ (mol/L)
MICP1	10 U	0.5	–	0.5
MICP2	10 U	0.5	–	0.05
CICP	–	–	0.5	0.5

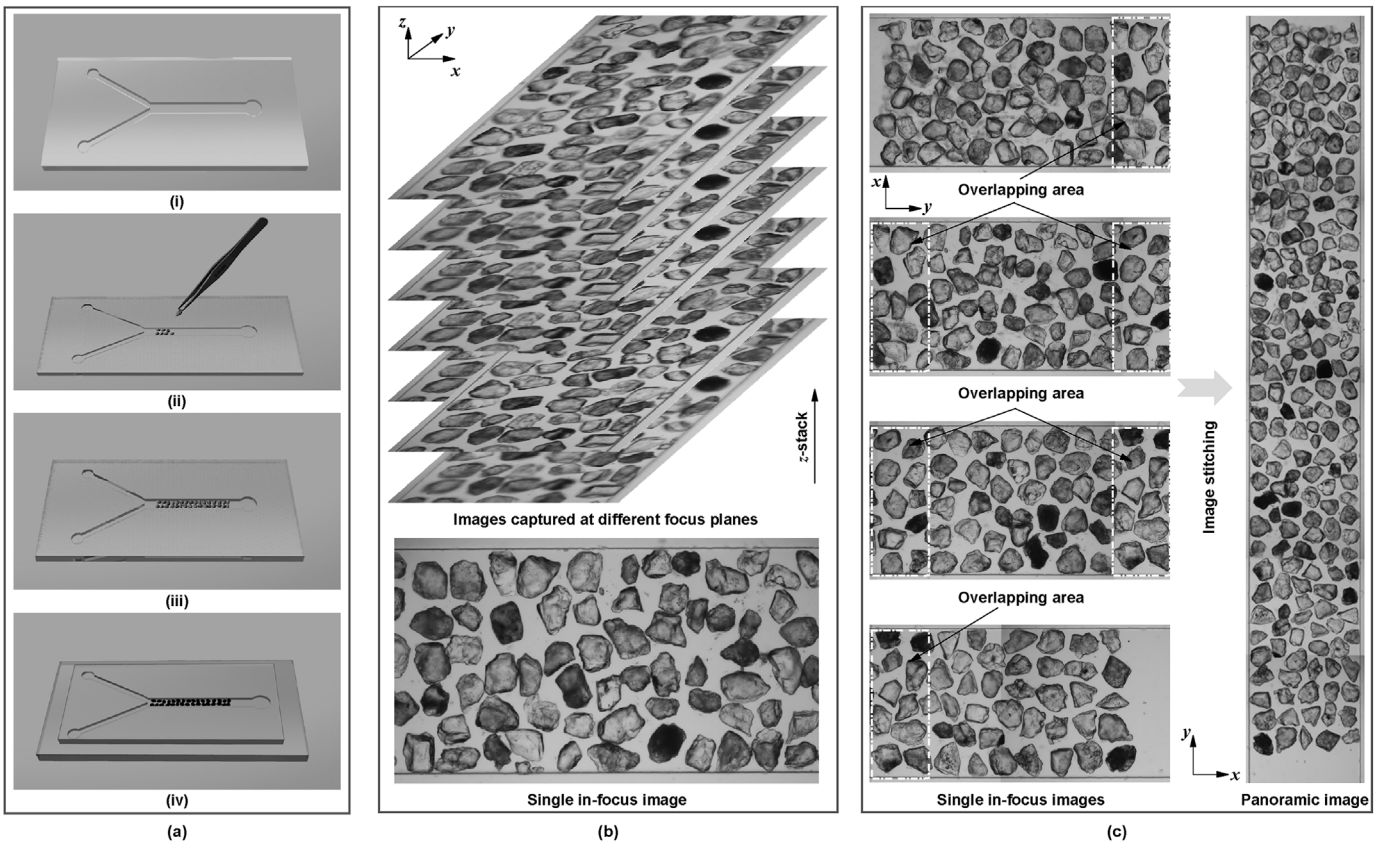

Fig. 1. (a) Fabrication process of the sand-containing microfluidic chip, and illustration of image-processing methods: (b) Extended depth of focus, and (c) Image stitching.

into the PDMS groove to construct a sand pack under a microscope. The length of the sand pack was approximately 6000 μm. The PDMS groove with sand particles was sealed with PDMS plate after surface treatment in a plasma cleaner for 90 s. The microchip was then bonded on a glass slide by surface treatment for 60 s. The glass slide was used as transparent support plate and would not contact with solution and sand particles. It should be noted that the design of this microchip aims to observe the process of precipitation through biological or chemical approaches at microscale. Although the boundary conditions for the microfluidic test, i.e. in a channel confined by PDMS walls, differ from that in field application, i.e. in soil matrix, it is still proper to use the microchip since the precipitated crystals are generally smaller than sand particles, and the PDMS material has limited impacts on the distribution of bacteria and the crystallization of calcium carbonate.

2.4. Test procedures

Saturation of the microchip is necessary as the air trapped in microchannels would significantly affect the distribution of calcium carbonate. Prior to reaction, the sand packs were saturated with degassed water by the following two steps. First, the microchips were immersed into the degassed water and vacuumed for around 10 min. The pore spaces of sand pack were filled with water due to capillary force. Second, the deionized water was injected into the microchannel at a flow rate of 100 μL/h. This step was intended to expel the air that might be trapped in large pores of the sand pack. Once the microchips were saturated, the inlets were connected to solution reservoirs and the microchip were mounted on the stage of microscope for biomineralization or mineralization tests. For biomineralization, the bacterial suspension and cementation solution were simultaneously injected into the microchip with a flow rate of 40 μL/h. For mineralization, the Na_2CO_3 and $CaCl_2$ solutions were injected at the same rate as that in the biomineralization test. The blotting papers were placed on the top of outlet to discharge the effluent during experiments. The details of test procedures are depicted in Fig. A2.

2.5. Image acquisition and processing

Images were captured by the inverted microscope with a 10 × objective lens. The work distance of this objective is 10 mm, the depth of field (DOF) of the object is around 4 μm, and the resolutions of each picture are 1920 pixels and 1200 pixels, corresponding to 1786 μm and 1116 μm, in horizontal and vertical directions, respectively. On one hand, the DOF of the object (i.e. 3.06 μm) was far less than the microchannel depth (i.e. 120 μm). Therefore, the images that lied outside the DOF would be blurred which hindered the evaluation of crystal distribution. The effect of limited DOF could be alleviated by moving the objective along *z*-axis to obtain a stack of images at different focal planes. On the other hand, as the length of sand pack was more than that of the captured picture, the objective needed to be shifted along the horizontal direction to obtain a full view of the sand pack. Instead of moving the objective, the microchip was moved by adjusting the stage of microscope along *y*-axis. It should be noted that for a given reaction time, the duration of imaging (i.e. the period of objective and stage moving) was less than 3 min to avoid significant occurrence of precipitates at imaging area.

For images with the same *x*- and *y*-coordinates, an image processing technique, called extended depth of focus, was adopted to obtain a single in-focus image with the software ImageJ (version 1.52p). Briefly, this image processing technique consists of making a *z*-stack image set and generating a fusion image by means of extended DOF algorithms (Aguet et al., 2008), as illustrated in

Fig. 1b. The panoramic image at a given reaction time could be stitched from four in-focus images arranged in a 1 × 4 grid by comparing the overlapping areas of adjacent tiles (Preibisch et al., 2009), as shown in Fig. 1c. For quantitative analysis, representative images were used to evaluate the distribution of crystals. Since the representative images were selected from the beginning, middle, and end sections of the whole sand pack and coved more than 60% of the panoramic image, it would be acceptable to characterize the distribution features with those images. The number of crystals was calculated manually using the software ImageJ.

3. Results

3.1. Visualization platform

Fig. 2 show the typical images of precipitates in the pore space for MICP1 (Fig. 2a), MICP2 (Fig. 2b) and CICP (Fig. 2c) tests, in the form of panoramic image. More images involving the evolution of precipitates in different tests were provided in Appendix A (see Figs. A3-A5). The results of biomineralization and mineralization show certain similarities yet large disparities during reaction. Both the biomineralization and mineralization processes involved the same reaction sequences: initiation of the flocculent materials (shown as the gray floc), formation of calcium carbonate crystals, and growth of crystals, leading to the clogging of pore space and the cementation of particles. The similarity indicates that the precipitation reaction, when calcium ions are combined with carbonate ions and precipitate calcium carbonate due to ionic bonding, plays a vital role in both biomineralization and mineralization processes. The crystals first appeared at the center of microchannel, which is analogous to the microfluidic tests without sand particles (Yin et al., 2009; Zeng et al., 2018), given that the presence of sand particles shaped a heterogeneous pore structure.

Although all tests show the existence of flocculation, the origination of flocs might be different. For mineralization (CIP, Fig. 2c), the flocs were mainly composed of amorphous calcium carbonate (ACC), an unstable precursor phase that could turn into crystalline polymorphs in supersaturation state (De Yoreo et al., 2015; Liu et al., 2020). For biomineralization (MICP1 and MICP2, Fig. 2a and b), the flocs could be the combination of ACC, calcium ions-bacterial cell aggregates, and ACC-bacterial cell aggregates, which make the nucleation and growth of calcium carbonate crystals be more complicated for MICP process. As those flocs would be transported by the flow of pore fluid, it is anticipated that the formation of flocs could hardly lead to the clogging of pores and thus has slight effects on the flow field. These flocs are more likely to be the feeding source of crystals. However, the direct identification of flocs constitutes requires further in situ techniques, such as synchrotron spectromicroscopy (Li et al., 2017; Sun et al., 2020).

3.2. Crystal growth and transverse distribution

The differences among different tests were further qualitatively analyzed in terms of initial time of bulk crystals (Fig. 2d–f), expanded width of crystals (w), (Fig. 2g–i), and expanded width normalized by the width of microchannel (Fig. 2j-l). For the

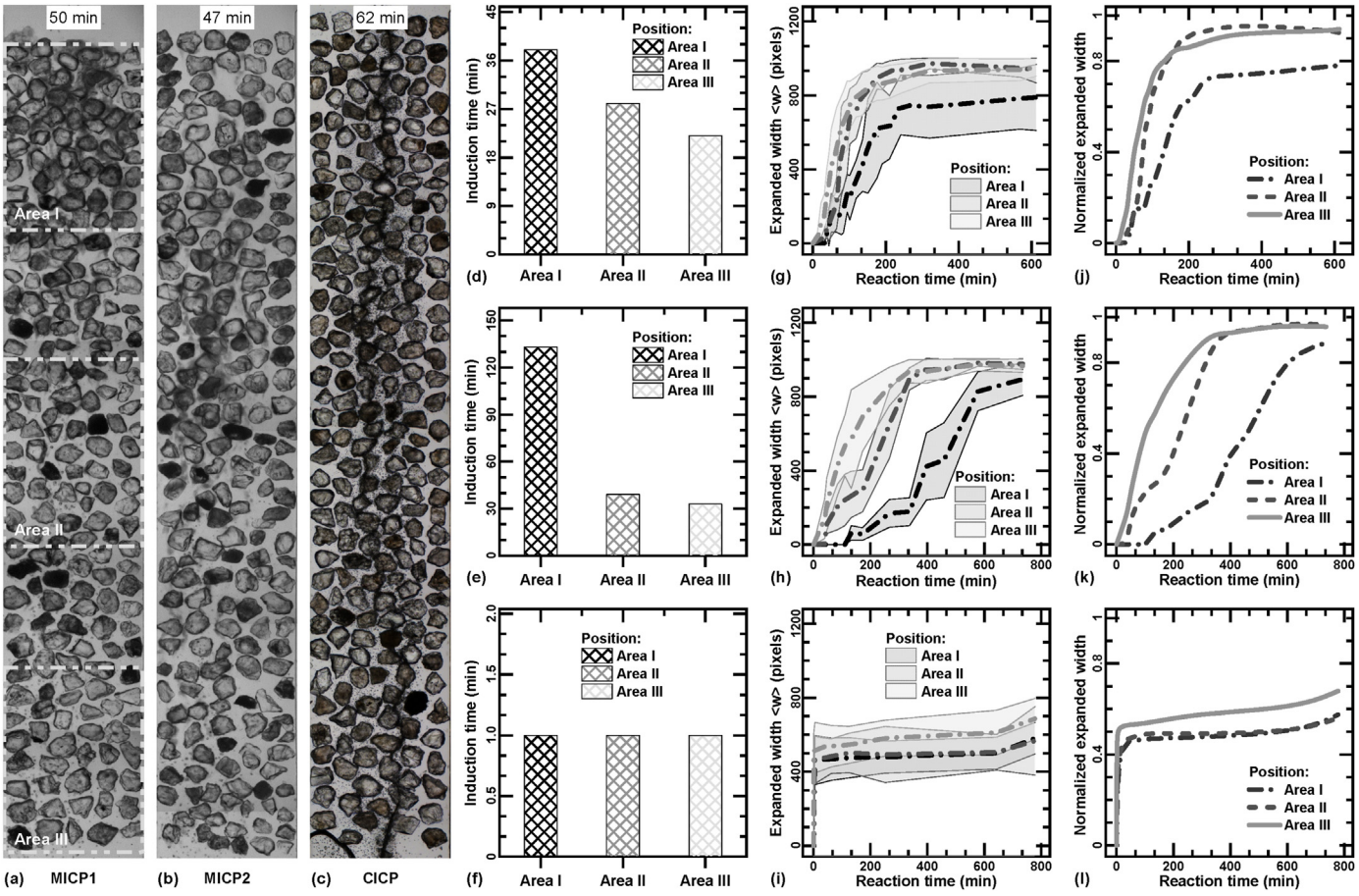

Fig. 2. Evolutions of pore spaces and crystal precipitates at different areas for (a) MICP1(0.5 mol/L Ca^{2+}), (b) MICP2(0.05 mol/L Ca^{2+}), and (C) CICP; induction time for (d) MICP1, (e) MICP2, and (f) CICP; expanded width for (g) MICP1, (h) MICP2, and (i) CICP; and average expanded width normalized by the width of microchannel for (j) MICP1, (k) MICP2, and (l) CICP.

convenience of calculation, the microchannel was divided into three areas (i.e. Areas I, II and III) at the beginning, middle, and end sections. The initial time refers to as the time between the injection of solutions and the first appearance of crystals in different areas, while the expanded width refers to as the vertical distance between the topmost and lowest crystals. For biomineralization tests, the crystals first precipitated in the Area III (more than 4000 μm away from the converging point) where the concentration of carbonate ions was higher than that in the other two areas due to a long mixing and reaction distance. The initial time decreased as the concentration of cementation solution increased. It took around 22 min and 33 min to precipitate bulk crystals for MICP1 and MICP2, respectively. The evolutions of representative bulk crystals among the pore space and pore throat (see Fig. 3) show that the crystals grow faster and larger for a high concentration of calcium ions, although the crystals may exhibit similar shapes as shown in Fig. 3a–d and i-l. Compared with biomineralization tests, however, the appearance of crystals in mineralization was almost spontaneous with the injection of solutions. Considering the crystallization pathway of calcium carbonate, the crystalline polymorphs were rapidly formed by the dehydration and aggregation of ACC, usually less than 30 min (Rodriguez-Blanco et al., 2011; De Yoreo et al., 2015). The retardation of crystal appearance for the MICP tests indicates that the MICP-formed ACC particles might be more stable than the CICP-formed ACC. The MICP-formed ACC particles were probably stabilized by the formed flocs, although the concentration of ACC particles might increase as the reaction increases. The accumulation of ACC particles in a given area in the reaction microchannel could be possibly attributed to the adsorption of flocs rather than the hydraulic reflex, since the solutions were continuously driven by syringe pump and the effluents were promptly discharged by the blotting papers.

The mean expanded width and standard deviation were calculated to exhibit the transvers precipitation behaviors and distribution of crystals. For all tests, due to the dispersion of solutes and tortuous of flow path, the crystals spread from an initial narrow band to a broad width as the reaction time increases. Generally, the mean expanded width far away from the inlet is greater than that near to the inlet. However, the evolution patterns of expanded width showed substantial differences between biomineralization and mineralization tests. The mean expanded width gradually increased and then became steady for both biomineralization tests, while it almost kept steady after a rapid increase in the first 5 min for mineralization test. The spreading of crystals in the mineralization test showed an instant evolution mode rather than a progressive mode in the biomineralization test. Apart from the evolution pattern, the distributions of crystals also showed a great disparity for the mineralization and biomineralization tests. The distributions of crystals for CICP test along both the reaction microchannel and cross-section were similar to those in its initial state. Even after reaction for 700 min, there were still some amounts of pore spaces not occupied by crystals, manifesting a heterogeneous distribution of crystals along the cross-section of the reaction microchannel. However, the distributions of crystals for biomineralization changed with reaction time and positions. A relative uniform distribution could be found in the Areas II and III

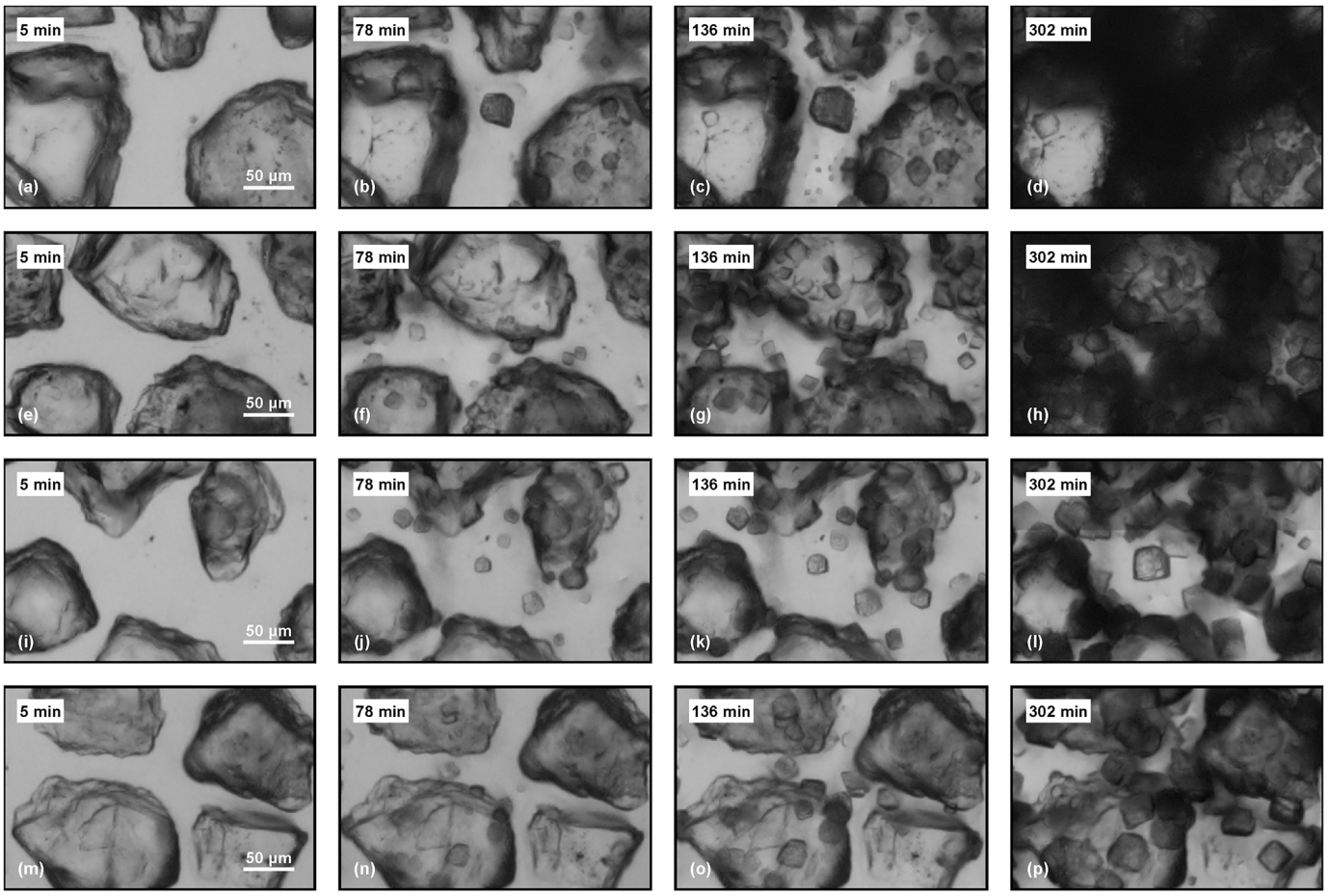

Fig. 3. Evolution of single crystals: (a)–(d) in the pore space and (e)–(h) at grain contact for MICP1; and (i)–(l) in the pore space and (e)–(h) at grain contact for MICP2 (scale bar: 50 μm).

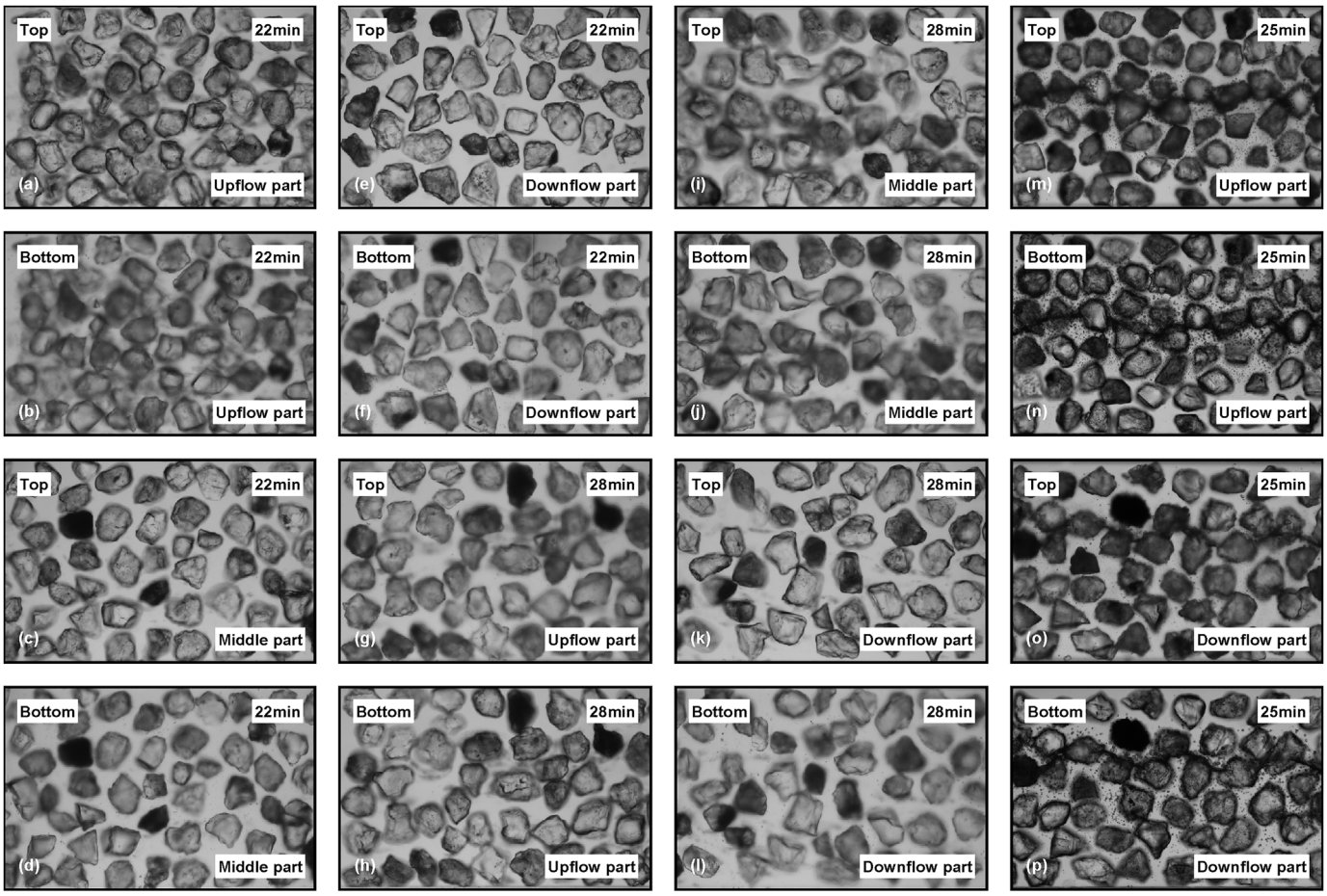

Fig. 4. Images of top and bottom faces at different areas: (a)–(f) for MICP1; (g)–(l) for MICP2; and (m)–(p) for CICP.

after 136 min and 337 min for 0.5 mol/L $CaCl_2$ and 0.05 mol/L $CaCl_2$, while the distributions in the Area I were uneven for both MICP1 and MICP2 during the whole period of test. The comparisons between MICP1 and MICP2 tests indicated that the effects of calcium ion concentration on the transverse expanding of crystals were mainly on the delay of crystal growth.

3.3. *Vertical distribution of $CaCO_3$ crystals*

The precipitated $CaCO_3$ crystals were distributed on the surface of sand-containing microchip after formation of the crystalline phases. For the sand-containing microchip, there were three surfaces available for the precipitation and could be classified as upper plane of reaction microchannel, bottom plane of reaction microchannel, and surface of sand particles. The upper and bottom planes are flat while the surface of sand particles is curved. Due to the depth of focus, it was difficult to calculate the number of crystals precipitated on the sand surface. A close investigation of the precipitation behaviors on the upper and bottom planes could characterize the vertical distribution of crystals in different tests. Fig. 4 shows some representative images of upper face and bottom plane for different tests, while more images at different reaction stages are shown in Figs. A6-A11. For both the MICP1 and MICP2 tests, the images of bottom plane and upper plane showed marginal difference, suggesting an observed uniform distribution of crystals along the vertical direction. It should be noted that the observed uniform distribution might be interfered by the large crystals captured from both the upper and bottom plane images. Since the crystals in the selected images were small in the projected area, it could be anticipated that those crystals were not large enough to occupy the cross-section of the main microchannels. Compared with the biomineralization tests, more crystals were precipitated on the bottom face than on the upper face in the mineralization test, manifesting a heterogeneous distribution along the depth of the microchannel.

The crystals precipitated on the upper or bottom plane were measured throughout the reaction periods to directly compare the nucleation behaviors of different tests. As shown in Fig. 5, the evolutions of number of crystals are consistent with the images in Fig. 4 and A6-A11. The lack of data after particular reaction time in the MICP1 and MICP2 tests was mainly due to the fact that the observed areas were coved by crystals and flocs. For biomineralization tests, the number of crystals increased with increasing reaction time. However, for mineralization test, the number of crystals almost kept constant after the initial time. As for different reaction areas, more crystals nucleated in the Area I for mineralization test compared with that in the Area III for biomineralization test. In addition, the distinction between upper and bottom planes was more obvious for mineralization test than that for biomineralization tests. Most of crystals were precipitated on the bottom plane in the CICP test.

4. Discussion

The formation of crystals from solutes includes a series of processes that involve the transformation of the solution phase to solid phase or crystalline phase. Various pathways have been proposed to interpret the mechanisms behind the processes of crystallization, including the classical nucleation and crystal growth theory in the aspect of monomer-by-monomer addition and nonclassical

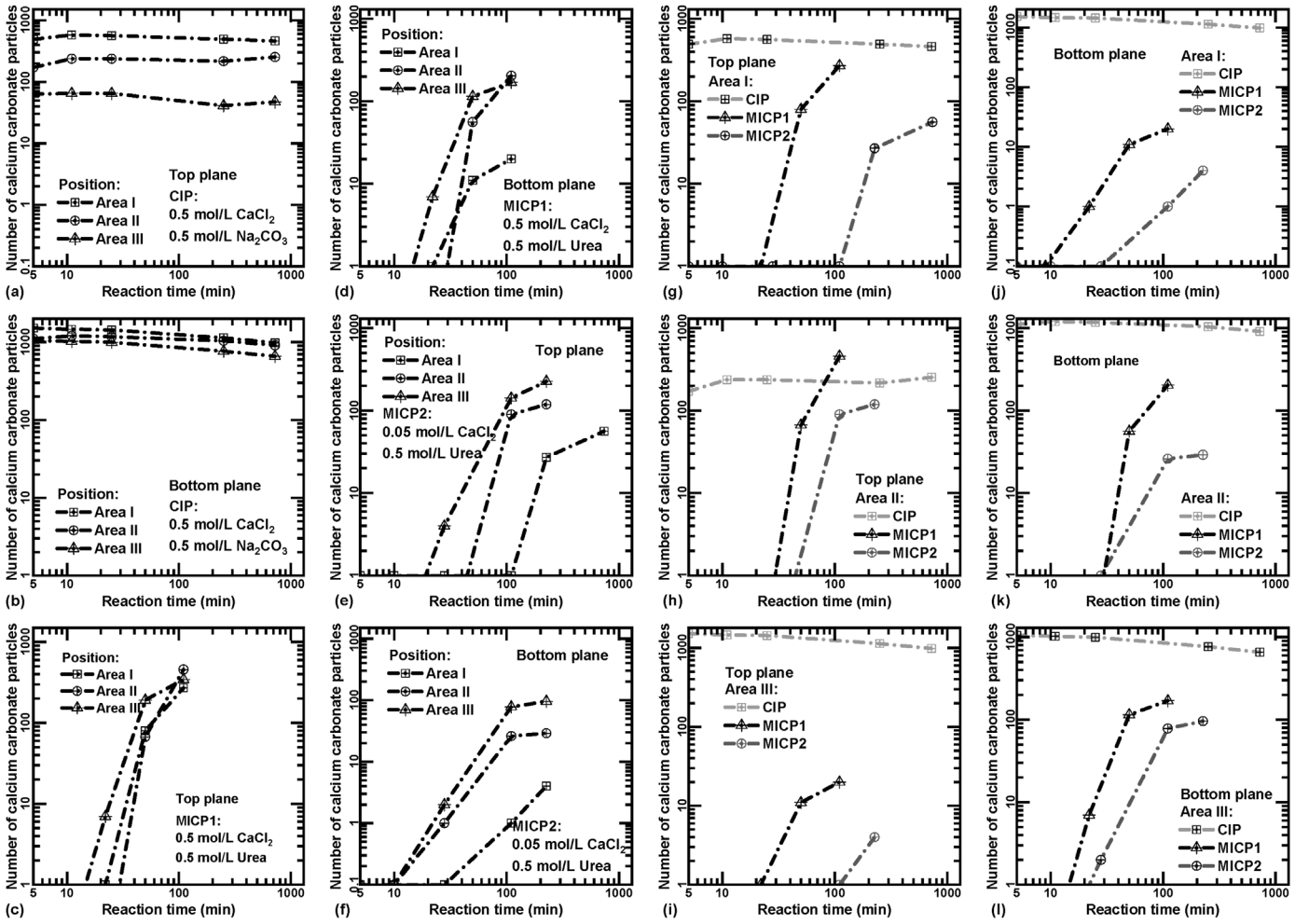

Fig. 5. Comparisons of number of crystals versus reaction time between different tests and different areas: (a–b) CICP, (c–d) MICP1, (e–f) MICP2, (g–i) top plane, and (j–l) bottom plane.

mechanisms in view of particle attachment (De Yoreo et al., 2015). The former theory (i.e. the classical nucleation and crystal growth theory) is the most mature description that enables to capture the crystallization behaviors by considering cross-scale interactions (Woehl et al., 2012; Carino et al., 2017). Mullin (2001) identified two nucleation modes, i.e. the primary nucleation and secondary nucleation, which is judged in the presence of crystalline matter in the reaction systems. For both modes, the supersaturation, a major contributor to chemical potential at a given temperature, could strongly affect the nucleation behaviors and subsequent crystal growth. The supersaturation index (σ) is frequently used to measure the supersaturated state, which can be expressed as $\sigma = c[CO_3^{2-}]c[Ca^{2+}]/K_{sp}$, where $c[CO_3^{2-}]$ and $c[Ca^{2+}]$ are the activities of carbonate and calcium ions (which could be approximated by the concentrations), and K_{sp} is the equilibrium activity of calcium carbonate (De Yoreo and Vekilov 2003). Due to the continuous injection of solutions, the values of σ in a particular area for a given test could be considered as constant during the initial reaction period when the flow path is not significantly affected by the precipitation. The value of σ for the MICP1 test is at least 10 times larger than that for the MICP2 test since the concentrations of carbonate ions are almost the same. In addition, the value of σ for CICP test is extremely larger than that for MICP1 test as the produce rate of carbonate ions would not exceed 14 mmol/min (corresponding to a urease activity of 14 U). The superhigh value of supersaturation index represents a large chemical potential or a high thermodynamic driving force, resulting in a fast and uncontrolled nucleation and growth of crystal as shown in the case of CICP test. Reducing the concentration of calcium ions could roughly lower the supersaturation index, leading to a more controllable nucleation and uniform distribution as proven by previous studies (Zeng et al., 2018; Xiao et al., 2022c). Apart from the concentration of calcium ions, adjusting the concentration of carbonate ions by regulating the urease activity of bacteria could also be an alternative to change the supersaturation index. An example was provided by Cheng et al. (2017), which suggested that a more effective precipitation pattern (the crystals are prone to aggregating and precipitating among particles) could be observed at a low urease activity. Another effect exerted by the high value of supersaturation index might be the occurrence of the secondary nucleation (Xu et al., 2020). The $CaCO_3$ crystals generated from primary nucleation could act as seed crystals to reduce the energy required for formation of the nuclei (Carino et al., 2017), manifesting the appearance of numerous crystals in the first 5 min of reaction for CICP test, as shown in Fig. 5.

The above discussions mainly focus on the thermodynamic aspect. The bacterial cell itself plays an important role in the MICP process due to its inertial particle and electrostatic characteristics (DeJong et al., 2010; Zhang et al., 2018). Although it has been controversial that whether the bacterial surfaces are the nucleation site of the calcium carbonate crystals (Terzis and Laloui, 2019), the changes of microenvironment adjacent to the cells are widely acknowledged for being alkalization and local supersaturated (Stocks-Fischer et al., 1999; Ferris et al., 2004). That means the

nucleation is most likely to occur in the microenvironment. In other words, the distribution of bacterial cells could significantly affect the positions where the $CaCO_3$ crystals precipitate (Xiao et al., 2022a). In the present study, the bacteria could adsorb on the surfaces of PDMS (Pan et al., 2022) and sand particles (Lutterodt et al., 2011) due to the van der Waals and Coulomb interaction (Zhong et al., 2017). The attached bacteria facilitate the formation of $CaCO_3$ crystals in the vicinity of bacterial cells. Consequently, the precipitated crystals on the upper and bottom surfaces are comparative for the biomineralization tests. It could also be inferred that more crystals are precipitated on the surfaces of sand particles due to the larger contact area. On the other hand, for the mineralization test, the $CaCO_3$ nuclei form on the surfaces of sand particles and walls of microchannel or in the solution by the heterogeneous and homogeneous nucleation. During the growth process, those nuclei are mainly under effects of the hydrodynamic interaction and gravity, promoting more crystals to be precipitated on the bottom surface as shown in Fig. 4 and Figs. A4-A9 in Appendix A. The above discussions indicate that the bacteria could regulate both the growth and distribution of $CaCO_3$ crystals, which partly demonstrates that the MICP process is a suitable cementation technology.

It should also be noted that the present study mainly focuses on the mechanisms of MICP in saturated state. However, various potential engineering applications for MICP utilization are initially in unsaturated conditions, such as ground improvement for subgrade and surface erosion reduction for sand slopes. It is thus important to figure out the mechanisms of MICP in unsaturated state. There are probably two main aspects that affect the MICP mechanisms due to initial water content. First, different initial water contents may result in different flow conditions affecting the delivery of solutions when injecting or percolating. Second, different initial water contents correspond to different air contents. When the pores are occupied by the air, the solutions tend to be condensed at the contacts of sand particles, leading to a more effective precipitation pattern (Cheng et al., 2013; Ahenkorah et al., 2022). Hence, the distribution and growth process of $CaCO_3$ in unsaturated state might differ from those in the present study. Future work may involve the process of MICP in unsaturated conditions.

5. Conclusions

A series of microfluidic tests is conducted to investigate the precipitation behaviors of both biomineralization and mineralization using the Y-shaped sand-containing microchips. Digital image processing methods are adopted to analyze the evolution of crystals as well the changes in the pore spaces. The distributions of $CaCO_3$ precipitates are quantitively measured in terms of the expanded width and number of crystals. The classical nucleation theory and hydrodynamic analysis are introduced to interpret the precipitation behaviors. The main conclusions can be drawn as follows:

(1) The sand-containing chip possess the ability to visualize the MICP process at high spatial and temporal resolutions. Both the MICP and CICP tests show a similar crystalline process, which is initiated by the formation of the flocculent materials. Then the calcium carbonate crystals appear and grow into large crystals. However, the periods for different stages have a great discrepancy, which is related to the reaction types (biomineralization or mineralization) and concentration of calcium ions.

(2) The induction time (the first appearance of crystal) for the mineralization test is much shorter than that for the biomineralization test with the same concentration of calcium ions. The $CaCO_3$ crystals first appear in the area far away from (more than 4000 μm) the converging point, and then spread to the whole microchannel for the biomineralization test; while for the mineralization test, the crystals form in different areas and show marginal differences throughout the microchannel.

(3) The crystalline behaviors of both the biomineralization and mineralization test could be well explained by the classical nucleation and crystal growth theory. The bacteria have a good performance in regulating the distribution of $CaCO_3$ crystals during MICP process.

Declaration of competing interest

The authors declare that they have no known competing financial interests or personal relationships that could have appeared to influence the work reported in this paper.

Acknowledgments

We acknowledge the funding support from the National Natural Science Foundation of China (Grant Nos. 51922024 and 52078085) and Chongqing Talents Program, China (Grant No. cstc2021ycjh-bgzxm0051).

Appendix A. Supplementary data

Supplementary data to this article can be found online at https://doi.org/10.1016/j.jrmge.2023.03.019.

References

Aguet, F., De Ville, D.V., Unser, M., 2008. Model-based 2.5-d deconvolution for extended depth of field in brightfield microscopy. IEEE Trans. Image Process. 17 (7), 1144–1153.

Ahenkorah, I., Rahman, M.M., Karim, M.R., Beecham, S., 2022. Unconfined compressive strength of MICP and EICP treated sands subjected to cycles of wetting-drying, freezing-thawing and elevated temperature: experimental and EPR modelling. J. Rock Mech. Geotech. Eng. https://doi.org/10.1016/j.jrmge.2022.08.007.

Carino, A., Testino, A., Andalibi, M.R., Pilger, F., Bowen, P., Ludwig, C., 2017. Thermodynamic-kinetic precipitation modeling. A case study: the amorphous calcium carbonate (ACC) precipitation pathway unravelled. Cryst. Growth Des. 17 (4), 2006–2015.

Cheng, L., Cord-Ruwisch, R., Shahin, M.A., 2013. Cementation of sand soil by microbially induced calcite precipitation at various degrees of saturation. Can. Geotech. J. 50 (1), 81–90.

Cheng, L., Shahin, M.A., Mujah, D., 2017. Influence of key environmental conditions on microbially induced cementation for soil stabilization. J. Geotech. Geoenviron. Eng. 143 (1), 11.

Chu, J., Ivanov, V., Stabnikov, V., Li, B., 2013. Microbial method for construction of an aquaculture pond in sand. Geotechnique 63 (10), 871–875.

Chu, J., Ivanov, V., Naeimi, M., Stabnikov, V., Liu, H.L., 2014. Optimization of calcium-based bioclogging and biocementation of sand. Acta Geotech. 9 (2), 277–285.

Cuthbert, M.O., McMillan, L.A., Handley-Sidhu, S., Riley, M.S., Tobler, D.J., Phoenix, V.R., 2013. A Field and modeling study of fractured rock permeability reduction using microbially induced calcite precipitation. Environ. Sci. Technol. 47 (23), 13637–13643.

Dagliya, M., Satyam, N., Sharma, M., Garg, A., 2022. Experimental study on mitigating wind erosion of calcareous desert sand using spray method for microbially induced calcium carbonate precipitation. J. Rock Mech. Geotech. Eng. 14 (5), 1556–1567.

de Anna, P., Pahlavan, A.A., Yawata, Y., Stocker, R., Juanes, R., 2020. Chemotaxis under flow disorder shapes microbial dispersion in porous media. Nat. Phys. 17 (1), 68–73.

De Yoreo, J.J., Vekilov, P.G., 2003. In: Dove, P.M., DeYoreo, J.J., Weiner, S. (Eds.), 3. Principles of Crystal Nucleation and Growth. Biomineralization, pp. 57–93. https://doi.org/10.1515/9781501509346-008.

De Yoreo, J.J., Gilbert, P.U.P.A., Sommerdijk, N.A.J.M., et al., 2015. Crystallization by particle attachment in synthetic, biogenic, and geologic environments. Science 349 (6247). https://doi.org/10.1126/science.aaa6760.

Dehkharghani, A., Waisbord, N., Dunkel, J., Guasto, J.S., 2019. Bacterial scattering in microfluidic crystal flows reveals giant active Taylor-Aris dispersion. Proc. Natl. Acad. Sci. U.S.A. 116 (23), 11119–11124.

DeJong, J.T., Mortensen, B.M., Martinez, B.C., Nelson, D.C., 2010. Bio-mediated soil improvement. Ecol. Eng. 36 (2), 197–210.

DeJong, J.T., Soga, K., Kavazanjian, E., et al., 2013. Biogeochemical processes and geotechnical applications: progress, opportunities and challenges. Geotechnique 63 (4), 287–301.
Ferris, F.G., Phoenix, V., Fujita, Y., Smith, R.W., 2004. Kinetics of calcite precipitation induced by ureolytic bacteria at 10 to 20 °C in artificial groundwater. Geochem. Cosmochim. Acta 68 (8), 1701–1710.
Gong, X., Wang, Y.W., Ihli, J., et al., 2015. The crystal hotel: a microfluidic approach to biomimetic crystallization. Adv. Mater. 27 (45), 7395–7400.
He, H., Chen, L., Wang, Z., et al., 2020. Screening the ion compositions on crystal morphology transitions by a microfluidic chip with a well-defined concentration gradient. Cryst. Growth Des. 20 (10), 6877–6887.
Kim, D.H., Mahabadi, N., Jang, J., van Paassen, L.A., 2020. Assessing the kinetics and pore-scale characteristics of biological calcium carbonate precipitation in porous media using a microfluidic chip experiment. Water Resour. Res. 56 (2), e2019WR025420.
Kirkland, C.M., Thane, A., Hiebert, R., et al., 2020. Addressing wellbore integrity and thief zone permeability using microbially-induced calcium carbonate precipitation (MICP): a field demonstration. J. Pet. Sci. Eng. https://doi.org/10.1016/j.petrol.2020.107060.
Lee, M., Gomez, M.G., El Kortbawi, M., Ziotopoulou, K., 2022. Effect of light biocementation on the liquefaction triggering and post-triggering behavior of loose sands. J. Geotech. Geoenviron. Eng. 148 (1), 04021170.
Li, S., Ihli, J., Marchant, W.J., et al., 2017. Synchrotron FTIR mapping of mineralization in a microfluidic device. Lab Chip 17 (9), 1616–1624.
Lin, H., Suleiman, M.T., Jabbour, H.M., et al., 2016. Enhancing the axial compression response of pervious concrete ground improvement piles using biogrouting. J. Geotech. Geoenviron. Eng. 142 (10), 04016045.
Liu, Z.M., Zhang, Z.S., Wang, Z.M., et al., 2020. Shape-preserving amorphous-to-crystalline transformation of $CaCO_3$ revealed by in situ TEM. Proc. Natl. Acad. Sci. U.S.A. 117 (7), 3397–3404.
Lutterodt, G., Foppen, J.W.A., Maksoud, A., Uhlenbrook, S., 2011. Transport of Escherichia coli in 25 m quartz sand columns. J. Contam. Hydrol. 119 (1–4), 80–88.
Ma, G., He, X., Jiang, X., Liu, H., Chu, J., Xiao, Y., 2021. Strength and permeability of bentonite-assisted biocemented coarse sand. Can. Geotech. J. 58 (7), 969–981.
Marzin, T., Desvages, B., Creppy, A., Lepine, L., Esnault-Filet, A., Auradou, H., 2020. Using microfluidic set-up to determine the adsorption rate of Sporosarcina Pasteurii bacteria on sandstone. Transport Porous Media 132 (2), 283–297.
Mitchell, J.K., Santamarina, J.C., 2005. Biological considerations in geotechnical engineering. J. Geotech. Geoenviron. Eng. 131 (10), 1222–1233.
Montoya, B.M., DeJong, J.T., 2015. Stress-strain behavior of sands cemented by microbially induced calcite precipitation. J. Geotech. Geoenviron. Eng. 141 (6), 04015019.
Montoya, B.M., Do, J., Gabr, M.A., 2021. Distribution and properties of microbially induced carbonate precipitation in underwater sand bed. J. Geotech. Geoenviron. Eng. 147 (10), 04021098.
Mullin, J.W., 2001. Crystallization, fourth ed. Butterworth-Heinemann, Oxford, UK.
Pan, F., Liu, M.D., Altenried, S., et al., 2022. Uncoupling bacterial attachment on and detachment from polydimethylsiloxane surfaces through empirical and simulation studies. J. Colloid Interface Sci. 622, 419–430.
Porter, H., Dhami, N.K., Mukherjee, A., 2018. Sustainable road bases with microbial precipitation. Proc. Inst. Civ. Eng.: Constr. Mater. 171 (3), 95–108.
Preibisch, S., Saalfeld, S., Tomancak, P., 2009. Globally optimal stitching of tiled 3D microscopic image acquisitions. J. Bioinform. 25 (11), 1463–1465.
Rodriguez-Blanco, J.D., Shaw, S., Benning, L.G., 2011. The kinetics and mechanisms of amorphous calcium carbonate (ACC) crystallization to calcite, viavaterite. Nanoscale 3 (1), 265–271.
Salifu, E., MacLachlan, E., Iyer, K.R., Knapp, C.W., Tarantino, A., 2016. Application of microbially induced calcite precipitation in erosion mitigation and stabilisation of sandy soil foreshore slopes: a preliminary investigation. Eng. Geol. 201, 96–105.
San Pablo, A.C.M., Lee, M., Graddy, C.M.R., et al., 2020. Meter-scale biocementation experiments to advance process control and reduce impacts: examining spatial control, ammonium by-product removal, and chemical reductions. J. Geotech. Geoenviron. Eng. 146 (11), 04020125.
Sharma, M., Satyam, N., Reddy, K.R., 2020. Strength enhancement and lead immobilization of sand using consortia of bacteria and blue-green algae. J. Hazard. Toxic Radioact. Waste 24 (4), 13.
Sharma, M., Satyam, N., Reddy, K.R., 2021. Rock-like behavior of biocemented sand treated under non-sterile environment and various treatment conditions. J. Rock Mech. Geotech. Eng. 13 (3), 705–716.
Sharma, M., Satyam, N., Reddy, K.R., 2022. Large-scale spatial characterization and liquefaction resistance of sand by hybrid bacteria induced biocementation. Eng. Geol. 302, 19.
Simatupang, M., Okamura, M., Hayashi, K., Yasuhara, H., 2018. Small-strain shear modulus and liquefaction resistance of sand with carbonate precipitation. Soil Dynam. Earthq. Eng. 115, 710–718.
Stocks-Fischer, S., Galinat, J.K., Bang, S.S., 1999. Microbiological precipitation of $CaCO_3$. Soil Biol. Biochem. 31 (11), 1563–1571.
Sun, C.Y., Stifler, C.A., Chopdekar, R.V., et al., 2020. From particle attachment to space-filling coral skeletons. Proc. Natl. Acad. Sci. U.S.A. 117 (48), 30159–30170.
Terzis, D., Laloui, L., 2019. A decade of progress and turning points in the understanding of bio-improved soils: a review. Geomech. Energy Environ. 19, 14.
Wang, Y.Z., Soga, K., DeJong, J.T., Kabla, A., 2019a. A microfluidic chip and its use in characterising the particle-scale behaviour of microbial-induced calcium carbonate precipitation (MICP). Geotechnique 69 (12), 1086–1094.
Wang, Y.Z., Soga, K., DeJong, J.T., Kabla, A.J., 2019b. Microscale visualization of microbial-induced calcium carbonate precipitation processes. J. Geotech. Geoenviron. Eng. 145 (9), 04021036.
Wang, Y.Z., Soga, K., DeJong, J.T., Kabla, A.J., 2021. Effects of bacterial density on growth rate and characteristics of microbial-induced $CaCO_3$ precipitates: particle-scale experimental study. J. Geotech. Geoenviron. Eng. 147 (6), 04021036.
Woehl, T.J., Evans, J.E., Arslan, L., Ristenpart, W.D., Browning, N.D., 2012. Direct in Situ determination of the mechanisms controlling nanoparticle nucleation and growth. ACS Nano 6 (10), 8599–8610.
Xiao, P., Liu, H.L., Xiao, Y., Stuedlein, A.W., Evans, T.M., 2018. Liquefaction resistance of bio-cemented calcareous sand. Soil Dynam. Earthq. Eng. 107, 9–19.
Xiao, Y., He, X., Evans, T.M., Stuedlein, A.W., Liu, H., 2019a. Unconfined compressive and splitting tensile strength of basalt fiber–reinforced biocemented Sand. J. Geotech. Geoenviron. Eng. 145 (9), 04019048.
Xiao, Y., Wang, Y., Desai, C.S., Jiang, X., Liu, H.L., 2019b. Strength and deformation responses of biocemented sands using a temperature-controlled method. Int. J. GeoMech. 19 (11), 10.
Xiao, Y., Stuedlein, A.W., Pan, Z.Y., et al., 2020. Toe-bearing capacity of precast concrete piles through biogrouting improvement. J. Geotech. Geoenviron. Eng. 146 (12), 06020026.
Xiao, Y., He, X., Wu, W., et al., 2021. Kinetic biomineralization through microfluidic chip tests. Acta Geotech 16 (10), 3229–3237.
Xiao, Y., Ma, G., Wu, H., Lu, H., Zaman, M., 2022a. Rainfall-induced erosion of biocemented graded slopes. Int. J. GeoMech. 22 (1), 04021256.
Xiao, Y., Xiao, W., Ma, G., He, X., Wu, H., Shi, J., 2022b. Mechanical performance of biotreated sandy road bases. J. Perform. Constr. Facil. 36 (1), 04021111.
Xiao, Y., He, X., Stuedlein, A.W., Chu, J., Evans, T.M., van Paassen, L.A., 2022c. Crystal growth of micp through microfluidic chip tests. J. Geotech. Geoenviron. Eng. 148 (5), 06022002.
Xu, S.J., Hou, Z.B., Chuai, X.Y., Wang, Y.F., 2020. Overview of secondary nucleation: from fundamentals to application. Ind. Eng. Chem. Res. 59 (41), 18335–18356.
Yin, H., Ji, B., Dobson, P.S., et al., 2009. Screening of biomineralization using microfluidics. Anal. Chem. 81 (1), 473–478.
Zamani, A., Montoya, B.M., Gabr, M.A., 2019. Investigating challenges of in situ delivery of microbial-induced calcium carbonate precipitation (MICP) in fine-grain sands and silty sand. Can. Geotech. J. 56 (12), 1889–1900.
Zambare, N.M., Naser, N.Y., Gerlach, R., Chang, C.B., 2020. Mineralogy of microbially induced calcium carbonate precipitates formed using single cell drop-based microfluidics. Sci. Rep. 10 (1), 17535.
Zeng, Y., Cao, J., Wang, Z., Guo, J., Lu, J., 2018. Formation of amorphous calcium carbonate and its transformation mechanism to crystalline $CaCO_3$ in laminar microfluidics. Cryst. Growth Des. 18 (3), 1710–1721.
Zhang, W., Ju, Y., Zong, Y., Qi, H., Zhao, K., 2018. In situ real-time study on dynamics of microbially induced calcium carbonate precipitation at a single-cell level. Environ. Sci. Technol. 52 (16), 9266–9276.
Zhong, H., Liu, G., Jiang, Y., et al., 2017. Transport of bacteria in porous media and its enhancement by surfactants for bioaugmentation: a review. Biotechnol. Adv. 35 (4), 490–504.

Dr. Yang Xiao was the "China Highly Cited Scholar" in 2022 for a fifth consecutive year and was awarded with one national second prize, two first awards of ministerial or provincial science and technology. He has published more than 160 papers in various journals such as *Journal of Geotechnical and Geoenvironmental Engineering* (ASCE) and *Chinese Journal of Geotechnical Engineering*. Dr. Xiao was the associate editor of *International Journal of Geomechanics* (ASCE) and the executive deputy Editor-in-Chief of *Biogeotechnics*. He also acts as editorial board members of eight well-known international journals, including *Canadian Geotechnical Journal* and *Soils and Foundations*. The research group headed by Dr. Xiao has made some achievements in the fields of static and dynamic characteristics and constitutive theory of soil, microscopic mechanism and mechanical characteristics of biocemented soil.